A thermo-hydro-mechanical finite-element model with freezing processes in saturated soils

Zheng, Tianyuan ; Miao, Xing-Yuan; Naumov, Dmitri ; Shao, Haibing ; Kolditz, Olaf ; Nagel, Thomas

Published in:
Environmental Geotechnics

Link to article, DOI:
10.1680/jenge.18.00092

Publication date:
2022

Document Version
Peer reviewed version

Submitted: 20 July 2018

Published online in 'accepted manuscript' format: 05 April 2019

Manuscript title: A Thermo-Hydro-Mechanical Finite Element Model with Freezing and Thawing Processes in Saturated Soils for Geotechnical Engineering

Authors: Tianyuan Zheng[1,2,3], Xing-Yuan Miao[1,2,4,] Dmitri Naumov[1], Haibing Shao[1,5], Olaf Kolditz[1,2], Thomas Nagel[1,6]

Affiliations: [1]Department of Environmental Informatics, Helmholtz Centre for Environmental Research – UFZ Permoserstr. 15, 04318 Leipzig, Germany. [2]Applied Environmental Systems Analysis, Technische Universität Dresden, Germany. [3]College of Engineering, Ocean University of China, Qingdao 266100, China. [4]Department of Energy Conversion and Storage, Technical University of Denmark, Risø Campus, Frederiksborgvej 399, 4000 Roskilde, Denmark. [5]Faculty of Geoscience, Geoengineering and Mining, Technische Universität Bergakademie Freiberg, Germany. [6]Department of Mechanical and Manufacturing Engineering, School of Engineering, Trinity College Dublin, College Green, Dublin, Ireland.

Corresponding author: Xing-Yuan Miao, Department of Environmental Informatics, Helmholtz Centre for Environmental Research – UFZ Permoserstr. 15, 04318 Leipzig, Germany. Tel.: +4915784563376

E-mail: ximi@dtu.dk

Accepted manuscript
doi: 10.1680/jenge.18.00092

Abstract

Freezing and thawing of soil are dynamic thermo-hydro-mechanical (THM) interacting coupled processes, and have attracted more and more attention due to their potentially severe consequences in geotechnical engineering. In this article, a fully-coupled thermo-hydro-mechanical freezing (THM-F) model is established for advanced system design and scenario analysis. The model is derived in the framework of the Theory of Porous Media (TPM), and solved numerically with the finite element method. Particularly, the derivation of theoretical aspects pertaining to the governing equations, especially including the thermo-mechanical decomposition treatment of the solid phase is presented in detail. Verification examples are provided from purely freezing (T-F), THM, and THM-F perspectives. Attention is paid to the heat and mass transfer, thermodynamic relations and the formation of frost heave. The migration of pore fluid from the unfrozen zone to the freezing area, and the blockage of pore space by ice lenses within the porous media are studied. The model is able to capture various coupled physical phenomena during freezing, e.g. the latent heat effect, groundwater flow alterations, as well as mechanical deformation.

Notation

Greek symbols

β_α thermal expansion coefficient of phase α [K^{-1}]

α_{FI} freezing expansion coefficient [-]

λ_α first Lamé coefficient of phase α [Nm^{-2}]

μ_α second Lamé coefficient of phase α [Nm^{-2}]

λ heat conductivity tensor [$Wm^{-1}\ K^{-1}$]

μ dynamic viscosity [Pa s]

ϕ_α volume fraction of phase α [-]

ϱ_α apparent density of phase α [kg m^{-3}]

$\varrho_{\alpha R}$ real (effective) density of phase α [kg m^{-3}]

Operators

div spatial divergence operator

grad spatial gradient operator

$(\bullet)'_\alpha$ material time derivative with respect to phase α

Roman symbols

c_p specific isobaric heat capacity [$Jkg^{-1}\ K^{-1}$]

h specific enthalpy [J kg^{-1}]

k coefficient of Sigmoid function [K^{-1}]

Δh_I specific enthalpy of ice fusion [J kg^{-1}]

K intrinsic permeability tensor [m^2]

p_{LR} liquid pressure [Pa]

$\mathbf{w}_{LS}$ seepage velocity [ms^{-1}]

k_α bulk modulus of phase α [Pa]

T_α temperature of phase α [K]

T_m freezing point temperature [K]

$\mathbf{v}_\alpha$ velocity of phase α [ms^{-1}]

Introduction

The thermal, hydraulic and mechanical behaviors of fluid-saturated porous media under varying thermal and mechanical loading with relevance to engineering constructions in permafrost (Jilin et al. 2003, Kurz et al. 2018, Wei et al. 2018), geotechnics (Zhou & Meschke 2013, Casini et al. 2016, Masoudian 2016), energy storage (Kabuth et al. 2016, Miao et al. 2019, 2017, 2016), and geothermal applications (Erol & François 2016, Zheng et al. 2016) are greatly influenced by frost action on time-scales ranging from daily to yearly cycles. For instance, in cold regions, the undisturbed soil temperature is often below 10 ˚C (Esen et al. 2009). Additional heat extraction by geotechnical activities such as geothermal heat pumps can thus lower the temperature below 0 ˚C to cause freezing, altering the hydraulic properties and the heat pump efficiency, even resulting in mechanical damage to the facilities.

To quantify the impact of freezing on an engineering scale, in this work, we develop a coupled thermo-hydro-mechanical freezing (THM-F) model based on macroscopic Theory of Porous Media (TPM) (Ehlers 2002, Bluhm et al. 2011, de Boer 1995), taking into account Truesdell's metaphysical principles.

The fundamental mathematical model based on mixture theory and thermodynamical principles was established for saturated porous media by Mikkola et al. (Mikkola & Hartikainen 2001). Coussy et al. (Coussy 2005) proposed another macroscopic ternary model incorporating liquid, ice and solid which was constructed based on the theory of poromechanics. Multon et al. (Multon et al. 2012) and (Neaupane et al. 1999) summarized the mechanical behavior of various numerical models and did a series of tests on the formation and

impact of crystals. As an extension of the above models, Zhou & Meschke (Zhou & Meschke 2013) developed a ternary model in view of a detailed physical description of ice crystallization. In recent years, TPM was developed from the previous mixture theory and poromechanics freezing phenomena and is considered to be a good framework for the multiphase freezing model. Under this framework, Bluhm and co-workers (Bluhm et al. 2011, 2008) presented a ternary model derived from thermodynamical considerations, employing the entropy inequality to identify the various dissipation mechanisms. Later, Lai et al. Lai et al. (2014) proposed a theoretical model of thermo-hydro-mechanical interactions during freezing and validated it with the help of experiments. In contrast with the above models, Koniorczyk et al. (Koniorczyk et al. 2015) introduced a linear damage model in conjunction with freezing processes. Recently, Na et al. (Na & Sun 2017) compared a THM freezing model based on finite strain theory to models using infinitesimal strain assumptions.

In the present paper, a fully coupled thermo-mechanically consistent THM-F model for liquid-saturated porous materials is derived based on the Theory of Porous Media by utilizing the entropy inequality. The basic of TPM related to theoretical aspects of the derivation of the current model have been partly described in Zheng et al. (Zheng et al. 2017). In contrast with previous models, Truesdell's metaphysical principles (Truesdell & Noll 2004) are exactly followed for the balance relations of the mixture. Different natural configurations are chosen to describe the mechanical behavior of ice and solid phases instead of a simple mixing material properties with empirical equations. This simplifies the establishment of material properties as consequences of phase properties and their separation from effects due to the phase change

itself. The entire solid deformation gradient is decomposed multiplicatively into a mechanical part and a thermal part rather than assuming the real density to be constant (Bluhm et al. 2014, Ricken & Bluhm 2010).

The detailed derivation is presented in Section 2 and Section 3. Verification examples are analyzed in Section 4 and Section 5. The main conclusions of this paper are stated in Section 6.

Mathematical model

In this section, we describe the mathematical derivation of the thermo-hydro-mechanical freezing model. Based on the model assumptions (Section 2.1) and saturation condition (Section 2.2), the balance equations are modified and processed. The deformation gradient of solid phase is split into mechanical part and thermal part (Section 2.3). The entropy inequality (Section 2.4) is used to derive certain relevant constitutive relations based on the Helmholtz free energy functions. With the derived constitutive relations, we are able to finalize the general balance equations into the specific governing equations. Our first implementation of the governing equations presented in this article are rest on the assumption of linear kinematics. It should be noticed that the descriptions of specific assumptions and part of intermediate derivation of our model have been presented in our previous work Zheng et al. (2017), we here maintain these parts for the sake of the integrity of derivation.

Assumptions

To specify the balance equations, the following basic assumptions should be first clarified Zheng et al. (2017).

Accepted manuscript
doi: 10.1680/jenge.18.00092

1. A three-phase mixture consisting of solid (S), ice (I) and the aqueous pore fluid (L) is considered in the current system: $\alpha = \{S, I, L\}$.
2. For all phases we assume incompressibility in the sense $\varrho_{\alpha R} = \varrho_{\alpha R}(T)$.
3. Deformation and flow occur in a quasi-static fashion such that inertial effects can be neglected in the governing equations: $\mathbf{a}_\alpha = \mathbf{0}$.
4. The local temperatures of all constituents are equal (local thermal equilibrium): $T_\alpha = T$.
5. Mass transfer is limited to the water and ice phases, i.e. $\hat{\varrho}_S = 0$, $\hat{\varrho}_L = -\hat{\varrho}_I$
6. The constituents solid and ice are kinematically constrained once the ice is formed at time t_F, i.e. $\mathbf{v}_S = \mathbf{v}_I$. At that stage, the solid may have undergone a motion already, i.e. the reference coordinates of an ice particle are given by $\hat{\mathbf{X}}_I = \boldsymbol{\chi}_S(X_S, t_F)$. The current placement of corresponding solid and ice particles is then given by the motion function of ice and solid via. $\mathbf{x} = \boldsymbol{\chi}_S(X_S, t) = \boldsymbol{\chi}_I(\hat{\mathbf{X}}_I, t) = \boldsymbol{\chi}_I(\boldsymbol{\chi}_S(\mathbf{X}_S, t_F), t)$

Where 6 is captured by a multiplicative decomposition of the deformation gradient of the solid into a part before freezing (S0) and a part after freezing (I) following Bluhm et al. (2011)

$$\mathbf{F}_S = \hat{\mathbf{F}}_I \mathbf{F}_{S0} \tag{1}$$

with the assumption that stresses in the ice are only determined by that part of the motion accrued after the occurrence of freezing, i.e. by $\hat{\mathbf{F}}_I$, while the stress response of the solid is characterized by $\mathbf{F}_S$. The decomposition of the motion in the context of small-strain assumption can be simplified as:

$$\boldsymbol{\epsilon}_S = \boldsymbol{\epsilon}_I + \boldsymbol{\epsilon}_{S0} \tag{2}$$

Based on the general mass balance in the form

$$\phi_\alpha(\varrho_{\alpha\mathrm{R}})'_\alpha + (\phi_\alpha)'_\alpha\varrho_{\alpha\mathrm{R}} + \varrho_{\alpha\mathrm{R}}\phi_\alpha \operatorname{div}\mathbf{v}_\alpha = \hat{\varrho}_\alpha \tag{3}$$

and Assumptions 5 and 6, the derivatives of the individual volume fractions can be written in the following form

$$(\phi_\mathrm{S})'_\mathrm{S} = -\phi_\mathrm{S}\operatorname{div}\mathbf{v}_\mathrm{S} - \phi_\mathrm{S}\frac{(\varrho_{\mathrm{SR}})'_\mathrm{S}}{\varrho_{\mathrm{SR}}} \tag{4}$$

$$(\phi_\mathrm{I})'_\mathrm{S} = \frac{\hat{\varrho}_\mathrm{I}}{\varrho_{\mathrm{IR}}} - \phi_\mathrm{S}\operatorname{div}\mathbf{v}_\mathrm{S} - \phi_\mathrm{I}\frac{(\varrho_{\mathrm{IR}})'_\mathrm{S}}{\varrho_{\mathrm{IR}}} \tag{5}$$

$$(\phi_\mathrm{L})'_\mathrm{S} = -\frac{\hat{\varrho}_\mathrm{I}}{\varrho_{\mathrm{LR}}} - \phi_\mathrm{L}\operatorname{div}\mathbf{v}_\mathrm{L} - \phi_\mathrm{L}\frac{(\varrho_{\mathrm{LR}})'_\mathrm{L}}{\varrho_{\mathrm{LR}}} - \operatorname{grad}\phi_\mathrm{L}\cdot\mathbf{w}_{\mathrm{LS}} \tag{6}$$

where the time derivative of the material density can be expressed based on Assumption 2 as

$$(\varrho_{\alpha\mathrm{R}})'_\alpha = \frac{\partial\varrho_{\alpha\mathrm{R}}}{\partial T}T'_\alpha = -\varrho_{\alpha\mathrm{R}}\beta_{T\alpha}T'_\alpha \tag{7}$$

with

$$\beta_{T\alpha} = -\frac{1}{\varrho_{\alpha\mathrm{R}}}\frac{\partial\varrho_{\alpha\mathrm{R}}}{\partial T} \tag{8}$$

Saturation condition

The saturation condition for this ternary mixture is written in absolute and in rate form (following the trajectory of the solid)

$$\sum_\alpha \phi_\alpha = 1 \tag{9}$$

$$\sum_\alpha (\phi_\alpha)'_\mathrm{S} = 0 \tag{10}$$

The mixture volume balance then can be expressed by the substitution of Eqs. (4)–(6) as

$$0 = \operatorname{div}[\mathbf{v}_\mathrm{S} + \phi_\mathrm{L}\mathbf{w}_{\mathrm{LS}}] + \hat{\varrho}_\mathrm{I}\left(\varrho_{\mathrm{LR}}^{-1} - \varrho_{\mathrm{IR}}^{-1}\right) + \frac{\phi_\mathrm{S}(\varrho_{\mathrm{SR}})'_\mathrm{S}}{\varrho_{\mathrm{SR}}} + \frac{\phi_\mathrm{I}(\varrho_{\mathrm{IR}})'_\mathrm{S}}{\varrho_{\mathrm{IR}}} + \frac{\phi_\mathrm{L}(\varrho_{\mathrm{LR}})'_\mathrm{L}}{\varrho_{\mathrm{LR}}} \tag{11}$$

Accepted manuscript
doi: 10.1680/jenge.18.00092

Decomposition of the solid deformation

According to Assumption 2, the solid phase is considered to be mechanically incompressible but undergo thermally induced volume changes. The entire deformation gradient can be decomposed multiplicatively into a mechanical (m) and a thermal part θ (see Fig. 1 and compare Graf (2008)).

$$\mathbf{F}_S = \mathbf{F}_{Sm}\mathbf{F}_{S\theta} \tag{12}$$

$$J_S = J_{Sm}J_{S\theta} \tag{13}$$

Since $J_S = \det\mathbf{F}_S$ and $\varrho_S^{0S} = \varrho_S \det\mathbf{F}_S$, in which ϱ_S^{0S} is the partial density of the solid phase in the reference configuration, the partial density of solid phase in the current configuration can be written as:

$$\varrho_S = \varrho_s^{0S} J_{S\theta}^{-1} J_{Sm}^{-1} \tag{14}$$

Since $\mathbf{F}_{S\theta}$ represents a measure for isotropic thermal deformations, $\varrho_S^{\theta} = \varrho_S^{0S} J_{S\theta}^{-1}$ is introduced as a short-hand parameter. This quantity can be understood as the partial density in the purely thermally loaded configuration B_θ (see Fig. 1). The densities of the respective configurations in Fig. 1 can be expressed with

$$\varrho_S^{0S} = \phi_S^{0S}\varrho_{SR}^{0S} \quad \text{in } B_0 \tag{15}$$

$$\varrho_S^{\theta} = \phi_S^{\theta}\varrho_{SR}^{\theta} \quad \text{in } B_\theta \tag{16}$$

$$\varrho_S = \phi_S\varrho_{SR} \quad \text{in } B \tag{17}$$

where ϱ_{SR}, ϱ_{SR}^{θ}, and ϱ_{SR}^{0S} are the real densities in B, B_θ, and B_0, respectively, whereas ϕ_S, ϕ_S^{θ} and ϕ_S^{0S} represent the corresponding solid volume fractions.

It is assumed that the mechanical part of the solid deformation gradient $\mathbf{F}_{Sm}$ (cf. Fig. 1)

Accepted manuscript
doi: 10.1680/jenge.18.00092

does not cause any change in the real density. Thus, for materially incompressible phases $\varrho_{\mathrm{SR}} = \varrho_{\mathrm{SR}}^{\theta}$. If we further assume that thermal loading results in purely homogeneous expansions, it can be shown by means of a simple illustration that during the transformations from B_0 into B_θ, bulk volume changes only occur due to variations in the real density and not due changes of volume fractions. Taken together, these considerations motivate the split Graf (2008)

$$\phi_{\mathrm{S}} = \phi_{\mathrm{S}}^{0\mathrm{S}} J_{\mathrm{Sm}}^{-1} \tag{18}$$

$$\varrho_{\mathrm{SR}} = \varrho_{\mathrm{SR}}^{0\mathrm{S}} J_{\mathrm{S}\theta}^{-1} \tag{19}$$

and hence

$$\varrho_{\mathrm{S}} = \left(\varrho_{\mathrm{SR}}^{\mathrm{S}0} \mathrm{J}_{\mathrm{S}\theta}^{-1}\right)\left(\phi_{\mathrm{S}}^{\mathrm{S}0} \mathrm{J}_{\mathrm{Sm}}^{-1}\right) \tag{20}$$

Furthermore, at this point an *a priori* constitutive relation for isotropic thermal expansion is introduced following

$$J_{\mathrm{S}\theta} = \exp\left(3\alpha_{T\mathrm{S}} \Delta T_{\mathrm{S}}\right) \tag{21}$$

Therein, $\alpha_{T\mathrm{S}}$ stands for the linear thermal expansion coefficient of the solid phase, and $\Delta T_{\mathrm{S}} = T - T_{\mathrm{S}}^{0\mathrm{S}}$, with $T_{\mathrm{S}}^{0\mathrm{S}}$ being the initial solid temperature in the reference configuration. The combination of Eqs. (19) and (21) yields the material density of the thermoelastic solid constituent as

$$\varrho_{\mathrm{SR}} = \varrho_{\mathrm{SR}}^{0\mathrm{S}} \exp\left(-3\alpha_{T\mathrm{S}} \Delta T_{\mathrm{S}}\right) \tag{22}$$

Assuming the thermal expansion of the ice phase and liquid phase also follow the above relation, we obtain

$$\varrho_{\alpha\mathrm{R}} = \varrho_{\alpha\mathrm{R}}^{0\alpha} \exp\left(-3\alpha_{T\alpha} \Delta T_{\alpha}\right) \tag{23}$$

Accepted manuscript
doi: 10.1680/jenge.18.00092

One can now show that the volumetric expansion coefficient defined in Eq. (8) is related to the linear thermal expansion coefficient by $\beta_{T\alpha} = 3\alpha_{T\alpha}$. If small thermal strains are assumed, the above relation can be linearized:

$$\varrho_{\alpha\mathrm{R}}^{\mathrm{lin}} = \varrho_{\alpha\mathrm{R}}^{0\alpha}(1 - 3\alpha_{T\alpha}\Delta T_\alpha) \tag{24}$$

Proceeding from Eqs. (13) and (21), one finds an explicit relation for the solid volume fraction as a function of temperature and the total deformation gradient

$$\phi_{\mathrm{S}} = \phi_{\mathrm{S}}^{0\mathrm{S}} J_{\mathrm{S}}^{-1} \exp\left(3\alpha_{T\mathrm{S}}\Delta T_{\mathrm{S}}\right) \tag{25}$$

Evaluation of the entropy inequality

The Coleman-Noll procedure is applied to exploit the entropy inequality. The expression can be formulated as

$$0 \leq \sum_{\alpha=1}^{\kappa} \Big\{ -\varrho_\alpha[(\psi_\alpha)'_\alpha + T'_\alpha \eta_\alpha] - \hat{\varrho}_\alpha \left(\psi_\alpha - \frac{1}{2}\mathbf{v}_\alpha \cdot \mathbf{v}_\alpha\right) + \boldsymbol{\sigma}_\alpha : \mathbf{l}_\alpha - \hat{\mathbf{p}}_\alpha \cdot \mathbf{v}_\alpha - \frac{1}{T}\mathbf{q}_\alpha \cdot \operatorname{grad} T - \lambda(\phi_\alpha)'_{\mathrm{S}} \Big\} \tag{26}$$

by assuming the local thermal equilibrium, invoking the production-term constraint in the energy balance, and adding the saturation condition as a constraint to the entropy inequality. Where the Lagrange multiplier λ can be understood as a pressure-type reaction force enforcing the saturation constraint.

We give the following *Ansatz* for the respective specific Helmholtz free energy functions associated with different phases in the mixture system based on the principle of phase-separation Ehlers (2002) and the assumptions in relation to the dependence of free energy of each phase on physical variables.

Accepted manuscript
doi: 10.1680/jenge.18.00092

$$\psi_{\mathrm{S}} = \psi_{\mathrm{S}}(\mathbf{C}_{\mathrm{S}}, T) \tag{27}$$

$$\psi_{\mathrm{I}} = \psi_{\mathrm{I}}(\widehat{\mathbf{C}}_{\mathrm{I}}, T, \phi_{\mathrm{I}}) \tag{28}$$

$$\psi_{\mathrm{L}} = \psi_{\mathrm{L}}(T) \tag{29}$$

where the right Cauchy-Green tensors $\mathbf{C}_{\mathrm{S}} = \mathbf{F}_{\mathrm{S}}^{\mathrm{T}}\mathbf{F}_{\mathrm{S}}$ and $\hat{\mathbf{C}}_{\mathrm{I}} = \hat{\mathbf{F}}_{\mathrm{I}}^{\mathrm{T}}\hat{\mathbf{F}}_{\mathrm{I}}$ are used.

Neglecting the terms associated with the kinetic energy of mass transfer, and applying the transformed mass balance equations Eqs. (4)–(6), Eq. (26) can be expanded to

$$\begin{aligned} 0 \leq & -\varrho_{\mathrm{S}}(\psi_{\mathrm{S}})'_{\mathrm{S}} + T'_{\mathrm{S}}\left(-\varrho_{\mathrm{S}}\eta_{\mathrm{S}} + \lambda\frac{\phi_{\mathrm{S}}}{\varrho_{\mathrm{SR}}}\frac{\partial\varrho_{\mathrm{SR}}}{\partial T}\right) - \varrho_{\mathrm{I}}(\psi_{\mathrm{I}})'_{\mathrm{S}} + T'_{\mathrm{S}}\left(-\varrho_{\mathrm{I}}\eta_{\mathrm{I}} + \lambda\frac{\phi_{\mathrm{I}}}{\varrho_{\mathrm{IR}}}\frac{\partial\varrho_{\mathrm{IR}}}{\partial T}\right) - \\ & - \varrho_{\mathrm{L}}(\psi_{\mathrm{L}})'_{\mathrm{L}} + T'_{\mathrm{L}}\left(-\varrho_{\mathrm{L}}\eta_{\mathrm{L}} + \lambda\frac{\phi_{\mathrm{L}}}{\varrho_{\mathrm{LR}}}\frac{\partial\varrho_{\mathrm{LR}}}{\partial T}\right) - \hat{\varrho}_{\mathrm{I}}\left(\psi_{\mathrm{I}} + \frac{\lambda}{\varrho_{\mathrm{IR}}} - \psi_{\mathrm{L}} - \frac{\lambda}{\varrho_{\mathrm{LR}}}\right) + \\ & + (\boldsymbol{\sigma}_{\mathrm{S}} + \lambda\phi_{\mathrm{S}}\mathbf{I}) : \mathbf{d}_{\mathrm{S}} + (\boldsymbol{\sigma}_{\mathrm{I}} + \lambda\phi_{\mathrm{I}}\mathbf{I}) : \mathbf{d}_{\mathrm{S}} + (\boldsymbol{\sigma}_{\mathrm{L}} + \lambda\phi_{\mathrm{L}}\mathbf{I}) : \mathbf{d}_{\mathrm{L}} - \\ & - \sum_{\alpha}\hat{\mathbf{p}}_{\alpha}\cdot\mathbf{v}_{\alpha} + \lambda\,\mathrm{grad}\,\phi_{\mathrm{L}}\cdot\mathbf{w}_{\mathrm{LS}} - \frac{1}{T}\mathbf{q}_{\mathrm{SIL}}\cdot\mathrm{grad}\,T \end{aligned} \tag{30}$$

with

$$\mathbf{q}_{\mathrm{SIL}} = \sum_{\alpha}\mathbf{q}_{\alpha} \tag{31}$$

We now introduce the terms $\boldsymbol{\sigma}_{\alpha}^{\mathrm{E}} = \boldsymbol{\sigma}_{\alpha} + \lambda\phi_{\alpha}\mathbf{I}$ defining the so-called extra stresses, due to their relatively small role compared with the momentum production due to fluid-solid interactions. Based on dimensional analysis, it is common practice to neglect fluid extra stresses. We find a hydrostatic stress state in the fluid and identify the Lagrange multiplier λ with the pore pressure p_{LR}:

$$\boldsymbol{\sigma}_{\mathrm{L}} = -p_{\mathrm{LR}}\phi_{\mathrm{L}}\mathbf{I} \tag{32}$$

with

$$\lambda = p_{\mathrm{LR}} \tag{33}$$

The constraint on the momentum production terms yields the relation

$$-(\hat{\mathbf{p}}_{\mathrm{S}}+\hat{\mathbf{p}}_{\mathrm{I}})=\hat{\mathbf{p}}_{\mathrm{L}}+\hat{\varrho}_{\mathrm{I}}\mathbf{w}_{\mathrm{LS}} \tag{34}$$

The extra momentum production is addressed as constitutively determined term in addition to effects contributed by the Lagrange multiplier–i.e. the liquid pressure–and is defined as

$$\hat{\mathbf{p}}_{\mathrm{L}}^{\mathrm{E}}=\hat{\mathbf{p}}_{\mathrm{L}}-\lambda\,\mathrm{grad}\,\phi_{\mathrm{L}} \tag{35}$$

Applying Eqs. (27)–(29) and $(\mathbf{C}_{\alpha})'_{\alpha}=2\mathbf{F}_{\alpha}^{\mathrm{T}}\mathbf{d}_{\alpha}\mathbf{F}_{\alpha}$, we can now write

$$\begin{aligned}0\leq&\left(\boldsymbol{\sigma}_{\mathrm{S}}^{\mathrm{E}}-2\varrho_{\mathrm{S}}\mathbf{F}_{\mathrm{S}}\frac{\partial\psi_{\mathrm{S}}}{\partial\mathbf{C}_{\mathrm{S}}}\mathbf{F}_{\mathrm{S}}^{\mathrm{T}}\right):\mathbf{d}_{\mathrm{S}}+\left(\boldsymbol{\sigma}_{\mathrm{I}}^{\mathrm{E}}-2\varrho_{\mathrm{I}}\hat{\mathbf{F}}_{\mathrm{I}}\frac{\partial\psi_{\mathrm{I}}}{\partial\hat{\mathbf{C}}_{\mathrm{I}}}\hat{\mathbf{F}}_{\mathrm{I}}^{\mathrm{T}}+\varrho_{\mathrm{I}}\phi_{\mathrm{I}}\frac{\partial\psi_{\mathrm{I}}}{\partial\phi_{\mathrm{I}}}\mathbf{I}\right):\mathbf{d}_{\mathrm{S}}-\\&-\sum_{\alpha}\varrho_{\alpha}\left(\eta_{\alpha}-\lambda\frac{1}{(\varrho_{\alpha\mathrm{R}})^{2}}\frac{\partial\varrho_{\alpha\mathrm{R}}}{\partial T}+\frac{\partial\psi_{\alpha}}{\partial T}\right)T'_{\alpha}-\\&\hat{\varrho}_{\mathrm{I}}\left[\psi_{\mathrm{I}}+\frac{1}{\varrho_{\mathrm{IR}}}\left(\lambda+\phi_{\mathrm{I}}\frac{\partial\psi_{\mathrm{I}}}{\partial\phi_{\mathrm{I}}}\right)-\psi_{\mathrm{L}}-\frac{\lambda}{\varrho_{\mathrm{LR}}}\right]-\\&-\varrho_{\mathrm{I}}\phi_{\mathrm{I}}\beta_{T\mathrm{I}}\frac{\partial\psi_{\mathrm{I}}}{\partial\phi_{\mathrm{I}}}T'_{\mathrm{S}}-\hat{\mathbf{p}}_{\mathrm{L}}^{\mathrm{E}}\cdot\mathbf{w}_{\mathrm{LS}}-\frac{1}{T}\mathbf{q}_{\mathrm{SIL}}\cdot\mathrm{grad}\,T\end{aligned} \tag{36}$$

This form motivates the introduction of the extra entropy terms $\eta_{\alpha}^{\mathrm{E}}$ such that

$$\eta_{\alpha}=\eta_{\alpha}^{\mathrm{E}}+\lambda\frac{1}{(\varrho_{\alpha\mathrm{R}})^{2}}\frac{\partial\varrho_{\alpha\mathrm{R}}}{\partial T}=\eta_{\alpha}^{\mathrm{E}}-\frac{\beta_{T\alpha}}{\varrho_{\alpha\mathrm{R}}}p_{\mathrm{LR}} \tag{37}$$

We then write the restrictions based on the *Ansatz* defined in Eqs. (27)–(29)

$$\eta_{\alpha}^{\mathrm{E}}=-\frac{\partial\psi_{\alpha}}{\partial T} \tag{38}$$

for α = S and L.

$$\eta_{\mathrm{I}}^{\mathrm{E,F}}=-\frac{\partial\psi_{\mathrm{I}}}{\partial T} \tag{39}$$

$$\eta_{\mathrm{I}}=\eta_{\mathrm{I}}^{\mathrm{E,F}}-\frac{\beta_{T\mathrm{I}}}{\varrho_{\mathrm{IR}}}\underbrace{\left(p_{\mathrm{LR}}+\varrho_{\mathrm{I}}\frac{\partial\psi_{\mathrm{I}}}{\partial\phi_{\mathrm{I}}}\right)}_{p_{\mathrm{red}}} \tag{40}$$

with

$$\eta_{\mathrm{I}}^{\mathrm{E,F}}=\eta_{\mathrm{I}}^{\mathrm{E}}+\frac{\beta_{T\mathrm{I}}}{\varrho_{\mathrm{IR}}}\varrho_{\mathrm{I}}\frac{\partial\psi_{\mathrm{I}}}{\partial\phi_{\mathrm{I}}} \tag{41}$$

$$\boldsymbol{\sigma}_{\mathrm{S}}=-p_{\mathrm{LR}}\phi_{\mathrm{S}}\mathbf{I}+2\varrho_{\mathrm{S}}\mathbf{F}_{\mathrm{S}}\frac{\partial\psi_{\mathrm{S}}}{\partial\mathbf{C}_{\mathrm{S}}}\mathbf{F}_{\mathrm{S}}^{\mathrm{T}} \tag{42}$$

$$\boldsymbol{\sigma}_{\mathrm{I}} = -\phi_{\mathrm{I}} \underbrace{\left(p_{\mathrm{LR}} + \varrho_{\mathrm{I}} \frac{\partial \psi_{\mathrm{I}}}{\partial \phi_{\mathrm{I}}} \right)}_{p_{\mathrm{red}}} \mathbf{I} + 2\varrho_{\mathrm{I}} \hat{\mathbf{F}}_{\mathrm{I}} \frac{\partial \psi_{\mathrm{I}}}{\partial \hat{\mathbf{C}}_{\mathrm{I}}} \hat{\mathbf{F}}_{\mathrm{I}}^{\mathrm{T}} \tag{43}$$

With the introduction of the chemical potential-type quantities

$$\Psi_{\mathrm{I}} = \psi_{\mathrm{I}} + \frac{p_{\mathrm{red}}}{\varrho_{\mathrm{IR}}} \tag{44}$$

and

$$\Psi_{\mathrm{L}} = \psi_{\mathrm{L}} + \frac{p_{\mathrm{LR}}}{\varrho_{\mathrm{LR}}} \tag{45}$$

the formulation of the remaining dissipation inequality can be written as

$$\mathcal{D} = -\hat{\mathbf{p}}_{\mathrm{L}}^{\mathrm{E}} \cdot \mathbf{w}_{\mathrm{LS}} - \frac{1}{T} \mathbf{q}_{\mathrm{SIL}} \cdot \operatorname{grad} T - \hat{\varrho}_{\mathrm{I}} (\Psi_{\mathrm{I}} - \Psi_{\mathrm{L}}) \geq 0 \tag{46}$$

Treating physically distinct terms independently, the heat flux vector and the flow-law can be found from the linear relation

$$0 \leq -\mathbf{q}_{\mathrm{SIL}} \cdot \operatorname{grad} T \quad \rightarrow \quad \mathbf{q}_{\mathrm{SIL}} = -\boldsymbol{\lambda}_{\mathrm{SIL}} \operatorname{grad} T \tag{47}$$

$$0 \leq -\hat{\mathbf{p}}_{\mathrm{L}}^{\mathrm{E}} \cdot \mathbf{w}_{\mathrm{LS}} \quad \rightarrow \quad \hat{\mathbf{p}}_{\mathrm{L}}^{\mathrm{E}} = -\mathbf{S}\mathbf{w}_{\mathrm{LS}} \tag{48}$$

with

$$\mathbf{a} \cdot \boldsymbol{\lambda}_{\mathrm{SIL}} \mathbf{a} \geq 0 \; \forall \; \mathbf{a} \neq \mathbf{0} \tag{49}$$

and

$$\mathbf{a} \cdot \mathbf{S}\mathbf{a} \geq 0 \; \forall \; \mathbf{a} \neq \mathbf{0} \tag{50}$$

where $\boldsymbol{\lambda}_{\mathrm{SIL}}$ is the effective heat conductivity tensor of the saturated porous medium.

We can recover a Darcy-like law by substituting the fluid stress tensor from Eq. (32) and the flow-law from relation (48) into the fluid momentum balance and choosing $\mathbf{S}^{-1} = \mathbf{K}/(\mu_{\mathrm{LR}} \phi_{\mathrm{L}}^2)$

$$\phi_{\mathrm{L}}\mathbf{w}_{\mathrm{LS}} = -\frac{\mathbf{K}}{\mu_{\mathrm{LR}}}\left(\operatorname{grad} p_{\mathrm{LR}} - \varrho_{\mathrm{LR}}\mathbf{b}_{\mathrm{L}}\right) \tag{51}$$

where **K** is the intrinsic permeability tensor, and varies with the ice formation which occupies the porosity. Finally, a kinetic law for the phase transition can be defined based on the difference in the chemical potentials of the liquid and ice phases

$$0 \leq -\hat{\varrho}_{\mathrm{I}}(\Psi_{\mathrm{I}} - \Psi_{\mathrm{L}}) \quad \rightarrow \quad \hat{\varrho}_{\mathrm{I}} = c_{\mathrm{F}}(\Psi_{\mathrm{L}} - \Psi_{\mathrm{I}}) \tag{52}$$

with

$$c_{\mathrm{F}} \geq 0 \tag{53}$$

The interested reader can refer to Ehlers & Häberle (2016) for an extended discussion of phase change in this context.

Governing equations

To test the various process couplings, we first implement the THM model based on linear kinematics before including geometric nonlinearities. The Helmholtz free energy functions for solid phase, ice phase and liquid phase in small strain setting are chosen as follows Graf (2008):

$$\begin{aligned}\varrho_{\mathrm{S}}^{0\mathrm{S}}\psi_{\mathrm{S}}^{\mathrm{lin}} = {} & \frac{1}{2}\lambda_{\mathrm{S}}(\boldsymbol{\epsilon}_{\mathrm{S}} : \mathbf{I})^2 + \mu_{\mathrm{S}}\boldsymbol{\epsilon}_{\mathrm{S}} : \boldsymbol{\epsilon}_{\mathrm{S}} - 3\alpha_{T\mathrm{S}}k_{\mathrm{S}}(T - T_{\mathrm{S}0})\boldsymbol{\epsilon}_{\mathrm{S}} : \mathbf{I} - \\ & \varrho_{\mathrm{S}}^{0\mathrm{S}}c_{\mathbf{E}\mathrm{S}}\left(T\ln\frac{T}{T_{\mathrm{S}0}} - T + T_{\mathrm{S}0}\right) - \varrho_{\mathrm{S}}^{0\mathrm{S}}\eta_{\mathrm{S}0}(T - T_{\mathrm{S}0})\end{aligned} \tag{54}$$

$$\begin{aligned}\varrho_{\mathrm{I}}^{0\mathrm{I}}\psi_{\mathrm{I}}^{\mathrm{lin}} = {} & \frac{1}{2}\lambda_{\mathrm{I}}(\boldsymbol{\epsilon}_{\mathrm{I}} : \mathbf{I})^2 + \mu_{\mathrm{I}}\boldsymbol{\epsilon}_{\mathrm{I}} : \boldsymbol{\epsilon}_{\mathrm{I}} - 3\alpha_{T\mathrm{I}}k_{\mathrm{I}}(T - T_{\mathrm{I}0})\boldsymbol{\epsilon}_{\mathrm{I}} : \mathbf{I} - \\ & \varrho_{\mathrm{I}}^{0\mathrm{I}}c_{\mathbf{E}\mathrm{I}}\left(T\ln\frac{T}{T_{\mathrm{I}0}} - T + T_{\mathrm{I}0}\right) - \varrho_{\mathrm{I}}^{0\mathrm{I}}\eta_{\mathrm{I}0}(T - T_{\mathrm{I}0}) - 3\alpha_{\mathrm{FI}}k_{\mathrm{I}}(\phi_{\mathrm{I}} - \phi_{\mathrm{I}0})\boldsymbol{\epsilon}_{\mathrm{I}} : \mathbf{I}\end{aligned} \tag{55}$$

$$\varrho_{\mathrm{L}}^{0\mathrm{L}}\psi_{\mathrm{L}}^{\mathrm{lin}} = -\varrho_{\mathrm{L}}^{0\mathrm{L}}c_{\mathbf{E}\mathrm{L}}\left(T\ln\frac{T}{T_{\mathrm{L}0}} - T + T_{\mathrm{L}0}\right) - \varrho_{\mathrm{L}}^{0\mathrm{L}}\eta_{\mathrm{L}0}(T - T_{\mathrm{L}0}) \tag{56}$$

Substituting the Helmholtz free energy functions (Eqs. (54)–(56)) into Eqs. (38) and (41),

Accepted manuscript
doi: 10.1680/jenge.18.00092

the exact constitutive relations are obtained. Together with the balance equations, we are able to approach the governing equations which consist of (i) the mixture volume balance

$$0 = \operatorname{div}\left(\mathbf{v}_{\mathrm{S}} + \phi_{\mathrm{L}}\mathbf{w}_{\mathrm{LS}}\right) - \beta_T T'_{\mathrm{S}} - \phi_{\mathrm{L}}\operatorname{grad}T \cdot \mathbf{w}_{\mathrm{LS}} \tag{57}$$

with

$$\beta_T = \sum_{\alpha} \phi_\alpha \beta_{T\alpha} \tag{58}$$

and

$$\phi_{\mathrm{L}}\mathbf{w}_{\mathrm{LS}} = -\frac{\mathbf{K}}{\mu_{\mathrm{LR}}}\left(\operatorname{grad}p_{\mathrm{LR}} - \varrho_{\mathrm{LR}}\mathbf{b}_{\mathrm{L}}\right) \tag{59}$$

(ii) the mixture momentum balance

$$\begin{aligned}\operatorname{div}\left[-p_{\mathrm{LR}}\mathbf{I} + \lambda_{\mathrm{S}}\operatorname{tr}(\boldsymbol{\epsilon}_{\mathrm{S}})\mathbf{I} + 2\mu_{\mathrm{S}}\boldsymbol{\epsilon}_{\mathrm{S}} - 3\alpha_{T\mathrm{S}}k_{\mathrm{S}}(T - T_{\mathrm{S}0})\mathbf{I} + \lambda_{\mathrm{I}}\operatorname{tr}(\boldsymbol{\epsilon}_{\mathrm{I}})\mathbf{I} + 2\mu_{\mathrm{I}}\boldsymbol{\epsilon}_{\mathrm{I}} - 3\alpha_{T\mathrm{I}}k_{\mathrm{I}}(T - T_{\mathrm{I}0})\mathbf{I}\right.\\ \left.-3\alpha_{\mathrm{FI}}k_{\mathrm{I}}(\phi_{\mathrm{I}} - \phi_{\mathrm{I}0} - \phi_{\mathrm{I}}\boldsymbol{\epsilon}_{\mathrm{I}} : \mathbf{I})\mathbf{I}\right] + \varrho\mathbf{b} = 0\end{aligned} \tag{60}$$

and (iii) the mixture energy balance

$$\left((\varrho c_p)^{\mathrm{eff}} - \frac{\partial \varrho_{\mathrm{I}}^{\mathrm{eq}}}{\partial T}\Delta h_{\mathrm{I}}\right)\frac{\partial T}{\partial t} - \operatorname{div}(\boldsymbol{\lambda}^{\mathrm{eff}}\operatorname{grad}T) + \varrho_{\mathrm{L}}c_{p\mathrm{L}}\mathbf{w}_{\mathrm{LS}} \cdot \operatorname{grad}T = 0 \tag{61}$$

The above governing equations have been implemented into the open-source finite element framework OpenGeoSys (Kolditz et al. 2012). The model is formulated in terms of the primary variables $\mathbf{u}$, p, and T which are approximated by linear (p, T) and quadratic $(\mathbf{u})$ shape functions, respectively. The system of equations is monolithically assembled and solved within an incremental-iterative Newton-Raphson scheme.

The ice volume fraction is determined based on an equilibrium approach and follows the relation (Zheng et al. 2016)

$$\phi_{\mathrm{I}} \equiv \phi_{\mathrm{I}}^{\mathrm{eq}} = \phi \frac{1}{1 + e^{-k(T - T_{\mathrm{m}})}} \tag{62}$$

Verification

To verify the numerical implementation of the fully coupled THM-F model developed in this contribution, two tests with analytical solutions reported in literature are first performed to demonstrate the modeling capability from purely freezing and THM perspective.

Freezing wall

This is a widely accepted benchmark for the validation of numerical models involving soil freezing. For example, Mottaghy and Rath Mottaghy & Rath (2006) developed a model for the permafrost in Poland. McKenzie et al. McKenzie et al. (2007) numerically investigated the freezing process in peat bogs. Both of them have adopted this benchmark. The numerical software TEMP/W recomended it for the validation of 1D freezing/thawing process. Rühaak Rühaak et al. (2015) included it in a series of benchmarks for the freezing simulation in porous media. In this benchmark, a 1 m long water column is connected to a freezing wall which is divided into 1000 small columns. Over time, the water in the vicinity of the wall slowly freezes. The propagation of the freezing front is calculated by the Neumann analytical solution Carslaw et al. (1962). The freezing front is defined as the edge between pure ice and the ice-water mixture. Since the analytical solution was developed for a pure phase change scenario, i.e. only water and ice, the porosity is set to 1.0 in our numerical model. The initial temperature is given as 273.15 K throughout the entire domain. At the position $x = 0$, a Dirichlet type boundary of temperature $T = 270.15\,\mathrm{K}$ is imposed, and is kept constant throughout the simulation. Picard

iterations are used for solving the nonlinearity with the absolute tolerance of 10^{-5}. Iterative solver BICGTAB is chosen for the linear system with the absolute tolerance of 10^{-16}. All parameters used in the model are listed in Table 1.

Here, the exponential function of Eq. (62) is applied to calculate the partial density of ice, with values ρ_{IR} = 1000 kg m $^{-3}$ [1], w = 2 K^{-1} and T_s = 269.15 K following Mottaghy and Rath Mottaghy & Rath (2006). Fig. 2a shows the evolution of the temperature profile during the freezing process. Different from a pure heat transfer process, there is a clear change in the temperature slope at the freezing point due to the latent heat effect and the change in thermal properties. The location of the phase change front $X(t)$ is compared with the analytical solution reported in Carslaw et al. (1962) in Fig. 2b. It can be seen that the numerical result corresponds well to the analytical solution.

Point heat source consolidation

Pore water typically has a higher thermal expansivity than the surrounding porous geomaterial. The temperature lift thus may be accompanied by an increase in pore pressure. If the domain is sufficiently permeable, these pore pressures will dissipate. The derivation of analytical solution can be found in Kolditz et al. (2012).

A two-dimensional axisymmetric model is set up for the verification. The model domain and meshes can be found in Fig. 3a. A point heat source is assigned as a Neumann boundary condition at the left bottom corner of the quarter. After the axisymmetric rotation around the

[1] This unphysical value is taken because of the constant volume assumption here to maintain the mass balance. The THM model accounts for expansion and will thus rely on physically appropriate density values.

vertical direction, the quarter is converted into a hemisphere. Since the point heat source for the sphere is set to 300 W in the analytical solution, the heat flux here for the hemisphere of the numerical model is thus 150 W. The radius of the domain is 10 m, and the initial temperature as well as pore pressure are 273K and 0 Pa, respectively. The model parameters can be found in Table 2. Direct solver SparseLU is applied for the linear system. Newton iteration is used for the nonlinear problem with the absolute tolerance of 10^{-5} for each primary variable. Three different observation locations are selected for the analytical and numerical solutions (0.25m, 0.5 m and 1 m from the injection source, Fig. 3b).

From Fig. 4 and Fig. 5, we can find a generally good match between the numerical solution and analytical solution. In Fig. 6, the discrepancy becomes larger with the further observation location because of the boundary effects and the density of the mesh which is very fine around the injection point and quickly becomes coarser and coarser along the radius. Since the chosen points are on the bottom boundary of the model, they do not have displacement in the *y* direction, the displacement of single point is only plotted on the *x* direction.

CIF test

In this section, we perform the so-called CIF-Test (Capillary suction, Internal damage and Freezing Thawing test) to further demonstrate the capability of our model. A cuboid solid specimen with a cross section of 15 cm and a height of 7.5 cm is considered. A detailed description including relevant parameters can be found in Table 3, (Setzer et al. 2001) and (Bluhm et al. 2014). Results reported in Bluhm et al. (Bluhm et al. 2014) based on the same testing serve as the basis for a qualitative verification of the model presented in this contribution.

Accepted manuscript
doi: 10.1680/jenge.18.00092

A Dirichlet boundary condition for temperature is applied at the bottom of the domain following the profile displayed in Fig. 7a. The bottom of the domain will be cooled linearly from 293.15 K to 253.15K in the first 4 hours, then kept constant for another 3 hours, followed by a heating phase up to 293.15 K in the final 5 hours. The bottom surface is sealed while all others are modeled as free draining boundaries. The finite element mesh and the displacement boundary conditions are shown in Fig. 7b. The time step size is set to 600 s. The SparseLU solver (Guennebaud, Jacob et al. 2010) is chosen to solve the linear system of equations, while the nonlinear solver absolute tolerances are set to 10^{-6} for displacements, 10^{-3} for temperature, 10^{-4} for pressure.

Fig. 8 shows the temperature distribution, ice volume fraction, and volume expansion fields at different times of the freezing-thawing cycle. During the initial 4 hours, the cooling process is taking place, decreasing temperature below the freezing point in certain regions of the specimen. Consequently, the phase change from liquid to ice occurs, and the volume strain reaches up to 4.5% which is half of the maximum volume deformation of 9% expected in the case of pure water. Later on, during the heating phase, the volume shrinks again due to thawing. Volume deformation and ice volume fractions are clearly co-localized. The results correspond well to those presented in Bluhm et al. (Bluhm et al. 2014) and Ricken et al. (Ricken & Bluhm 2010).

In Fig. 9, we discuss the fluid pressure distribution on different time point and varied permeability. In the simulations leading to Figs. 9a and 9b, the permeability is assumed to be constant and does not vary due to the formation of ice. Due to freezing process, the liquid

pressure turns to negative in the vicinity of the freezing zone, and the water is sucked to the freezing front. In contrast, thawing leads to a contraction of the matrix such that water is expelled from the domain. In Figs. 9c and 9d, the permeability change due to pore blockage is considered by introducing a relative permeability and linking it to the ice volume fraction $k_{\mathrm{r}}(\check{\phi_{\mathrm{I}}}) = 10^{-\Omega\phi(1-\phi_{\mathrm{I}}/\check{\phi})}$ (Rühaak et al. 2015). While similar flow patterns as described above remain, the permeability decreases dramatically due to ice formation and an impermeable zone forms in the freezing area. This effect is technically exploited when freezing barriers against contaminant transport are established (Peters 1995).

Conclusions

In this paper, a ternary macroscopic model within the framework of the Theory of Porous Media has been presented for the simulation of freezing and thawing cycles in liquid saturated porous media. The model includes latent heat effects, volume expansion due to ice formation, associated flow mechanisms and permeability changes due to the alterations of porosity. A freezing wall benchmark and a point heat source consolidation test were used for the quantitative verification of the implemented model through comparison with the analytical solution from purely freezing and THM perspective. A CIF test was applied to verify the implementation of the fully coupled THM-F model by qualitatively comparing the results to Bluhm et al.'s work (Bluhm et al. 2014).

References

Bluhm, J., Bloßfeld, W. M. & Ricken, T. (2014), 'Energetic effects during phase transition under freezing-thawing load in porous media–a continuum multiphase description and fe-simulation', *ZAMM-Journal of Applied Mathematics and Mechanics/Zeitschrift für Angewandte Mathematik und Mechanik* **94**(7-8), 586–608.

Bluhm, J., Ricken, T. & Bloßfeld, W. M. (2008), 'Energetische aspekte zum gefrierverhalten von wasser in porösen strukturen', *PAMM* 8(1), 10483–10484. URL: http://dx.doi.org/10.1002/pamm.200810483

Bluhm, J., Ricken, T. & Bloßfeld, M. (2011), Ice Formation in Porous Media, *in* B. Markert, ed., 'Advances in Extended and Multifield Theories for Continua', Vol. 59 of *Lecture Notes in Applied and Computational Mechanics*, Springer Berlin Heidelberg, pp. 153–174. URL: http://dx.doi.org/10.1007/978-3-642-22738-7_8

Carslaw, H. S., Jaeger, J. C. & Feshbach, H. (1962), 'Conduction of heat in solids', *Physics Today* **15**, 74.

Casini, F., Gens Solé, A., Olivella Pastallé, S. & Viggiani, G. (2016), 'Artificial ground freezing of a volcanic ash: laboratory tests and modelling', *Environmental Geotechnics* **3**(3), 1–14.

Coussy, O. (2005), 'Poromechanics of freezing materials', *Journal of the Mechanics and Physics of Solids* **53**(8), 1689–1718.

de Boer, R. (1995), 'Thermodynamics of Phase Transitions in Porous Media', *Applied Mechanics Reviews* **48**(10), 613–622. URL: http://dx.doi.org/10.1115/1.3005042

Ehlers, W. (2002), Foundations of multiphasic and porous materials, *in* W. Ehlers & J. Bluhm, eds, 'Porous Media: Theory, Experiments and Numerical Applications', Springer, Berlin, pp. 4–86.

Ehlers, W. & Häberle, K. (2016), 'Interfacial mass transfer during gas–liquid phase change in deformable porous media with heat transfer', *Transport in Porous Media* **114**(2),

525–556.

Erol, S. & François, B. (2016), 'Freeze damage of grouting materials for borehole heat exchanger: Experimental and analytical evaluations', *Geomechanics for Energy and the Environment* **5**, 29–41.

Esen, H., Inalli, M. & Esen, Y. (2009), 'Temperature distributions in boreholes of a vertical ground-coupled heat pump system', *Renewable Energy* **34**(12), 2672–2679.

Graf, D.-I. T. (2008), Multiphasic flow processes in deformable porous media under consideration of fluid phase transitions, PhD thesis, Universität Stuttgart.

Guennebaud, G., Jacob, B. et al. (2010), 'Eigen v3', http://eigen.tuxfamily.org.

Jilin, Q., Jianming, Z. & Yuanlin, Z. (2003), 'Influence of freezing-thawing on soil structure and its soil mechanics significance', *Chinese Journal of Rock Mechanics and Engineering* **22**(2), 690–2.

Kabuth, A., Dahmke, A., Beyer, C., Bilke, L., Dethlefsen, F., Dietrich, P., Duttmann, R., Ebert, M., Feeser, V., Görke, U.-J., Köber, R., Rabbel, W., Schanz, T., Schäfer, D., Würdemann, H. & Bauer, S. (2016), 'Energy storage in the geological subsurface: dimensioning, risk analysis and spatial planning: the angus+ project', *Environmental Earth Sciences* **76**(1), 23. URL: http://dx.doi.org/10.1007/s12665-016-6319-5

Kolditz, O., Bauer, S., Bilke, L., Böttcher, N., Delfs, J. O., Fischer, T., Görke, U. J., Kalbacher, T., Kosakowski, G., McDermott, C. I., Park, C. H., Radu, F., Rink, K., Shao, H., Shao, H. B., Sun, F., Sun, Y. Y., Singh, A. K., Taron, J., Walther, M., Wang, W., Watanabe, N., Wu, Y., Xie, M., Xu, W. & Zehner, B. (2012), 'Opengeosys: an open-source initiative for numerical simulation of thermo-hydro-mechanical/chemical (thm/c) processes in porous media', *Environmental Earth Sciences* **67**(2), 589. URL: http://dx.doi.org/10.1007/s12665-012-1546-x

Koniorczyk, M., Gawin, D. & Schrefler, B. A. (2015), 'Modeling evolution of frost damage in fully saturated porous materials exposed to variable hygro-thermal conditions', *Computer Methods in Applied Mechanics and Engineering* **297**, 38–61.

Kurz, D., Flynn, D., Alfaro, M., Arenson, L. U. & Graham, J. (2018), 'Seasonal deformations under a road embankment on degrading permafrost in northern canada', *Environmental Geotechnics* pp. 1– 12.

Lai, Y., Pei, W., Zhang, M. & Zhou, J. (2014), 'Study on theory model of hydro-thermal–mechanical interaction process in saturated freezing silty soil', *International Journal of Heat and Mass Transfer* **78**, 805–819.

Masoudian, M. S. (2016), 'Multiphysics of carbon dioxide sequestration in coalbeds: A review with a focus on geomechanical characteristics of coal', *Journal of Rock Mechanics and Geotechnical Engineering* **8**(1), 93–112.

McKenzie, J. M., Voss, C. I. & Siegel, D. I. (2007), 'Groundwater flow with energy transport and water–ice phase change: numerical simulations, benchmarks, and application to freezing in peat bogs', *Advances in Water Resources* **30**(4), 966–983.

Miao, X.-Y., Beyer, C., Görke, U.-J., Kolditz, O., Hailemariam, H. & Nagel, T. (2016), 'Thermo-hydro-mechanical analysis of cement-based sensible heat stores for domestic applications', *Environmental Earth Sciences* **75**(18), 1293.

Miao, X.-Y., Kolditz, O. & Nagel, T. (2019), 'Modelling thermal performance degradation of high and low-temperature solid thermal energy storage due to cracking processes using a phase-field approach', *Energy Conversion and Management* **180**, 977–989.

Miao, X.-Y., Zheng, T., Görke, U.-J., Kolditz, O. & Nagel, T. (2017), 'Thermo-mechanical analysis of heat exchanger design for thermal energy storage systems', *Applied Thermal Engineering* **114**, 1082–1089.

Mikkola, M. & Hartikainen, J. (2001), 'Mathematical model of soil freezing and its numerical implementation', *International Journal for Numerical Methods in Engineering* **52**(5-6), 543–557.

Mottaghy, D. & Rath, V. (2006), 'Latent heat effects in subsurface heat transport modelling and their impact on palaeotemperature reconstructions', *Geophysical Journal International* **164**(1), 236–245.

Multon, S., Sellier, A. & Perrin, B. (2012), 'Numerical analysis of frost effects in porous media. benefits and limits of the finite element poroelasticity formulation', *International Journal for Numerical and Analytical Methods in Geomechanics* **36**(4), 438–458.

Na, S. & Sun, W. (2017), 'Computational thermo-hydro-mechanics for multiphase freezing and thawing porous media in the finite deformation range', *Computer Methods in Applied Mechanics and Engineering* **318**, 667–700.

Neaupane, K., Yamabe, T. & Yoshinaka, R. (1999), 'Simulation of a fully coupled thermo–hydro– mechanical system in freezing and thawing rock', *International Journal of Rock Mechanics and Mining Sciences* **36**(5), 563–580.

Peters, R. P. (1995), 'Open frozen barrier flow control and remediation of hazardous soil'. US Patent 5,416,257.

Ricken, T. & Bluhm, J. (2010), 'Modeling fluid saturated porous media under frost attack', *GAMM-Mitteilungen* **33**(1), 40–56. URL: http://dx.doi.org/10.1002/gamm.201010004

Rühaak, W., Anbergen, H., Grenier, C., McKenzie, J., Kurylyk, B. L., Molson, J., Roux, N. & Sass, I. (2015), 'Benchmarking numerical freeze/thaw models', *Energy Procedia* **76**, 301–310.

Setzer, M., Auberg, R., Kasparek, S., Palecki, S. & Heine, P. (2001), 'Cif-test-capillary suction, internal damage and freeze thaw test', *Materials and Structures* **34**(9), 515–525.

Truesdell, C. & Noll, W. (2004), The Non-Linear Field Theories of Mechanics, *in* S. Antman, ed., 'The Non-Linear Field Theories of Mechanics', Springer Berlin Heidelberg, pp. 1–579. URL: http://dx.doi.org/10.1007/978-3-662-10388-3_1

Wei, X., Niu, Z., Li, Q. & Ma, J. (2018), 'Potential failure analysis of thawing-pipeline interaction at fault crossing in permafrost', *Soil Dynamics and Earthquake Engineering* **106**, 31–40.

Zheng, T., Miao, X.-Y., Naumov, D., Shao, H., Kolditz, O. & Nagel, T. (2017), A thermo-hydro-mechanical finite element model of freezing in porous media—thermo-mechanically consistent formulation and application to ground source

heat pumps, *in* 'Proceedings of the VII International Conference on Coupled Problems in Science and Engineering', pp. 1008–1019.

Zheng, T., Shao, H., Schelenz, S., Hein, P., Vienken, T., Pang, Z., Kolditz, O. & Nagel, T. (2016), 'Efficiency and economic analysis of utilizing latent heat from groundwater freezing in the context of borehole heat exchanger coupled ground source heat pump systems', *Applied Thermal Engineering* **105**, 314–326.

Zhou, M. & Meschke, G. (2013), 'A three-phase thermo-hydro-mechanical finite element model for freezing soils', *International Journal for Numerical and Analytical Methods in Geomechanics* **37**(18), 3173–3193.

Accepted manuscript
doi: 10.1680/jenge.18.00092

Table 1. Parameters used in the freezing wall benchmark, following the configuration proposed by Mottaghy and Rath Mottaghy & Rath (2006)

Parameter	Value	Unit
Grid size	0.001	m
Initial temperature	273.15	K
Boundary temperature	270.15	K
Porosity	1	-
Water heat capacity	4179	$J\,kg^{-1}\,K^{-1}$
Water thermal conductivity	0.613	$W\,m^{-1}\,K^{-1}$
Water density	1000	$kg\,m^{-3}$
Ice heat capacity	2052	$J\,kg^{-1}\,K^{-1}$
Ice thermal conductivity	2.14	$W\,m^{-1}\,K^{-1}$
Ice density	1000	$kg\,m^{-3}$
Time step size	864	sec
Total simulation time	100	day

Accepted manuscript
doi: 10.1680/jenge.18.00092

Table 2. Parameters for the point heat source consolidation

Parameter	Value	Unit
Initial temperature	273.15	K
Porosity	0.16	-
Water specific heat capacity	4280	$J\,kg^{-1}\,K^{-1}$
Water thermal conductivity	0.56	$W\,m^{-1}\,K^{-1}$
Water real density	1000	$kg\,m^{-3}$
Solid specific heat capacity	1000	$J\,kg^{-1}\,K^{-1}$
Solid thermal conductivity	1.64	$W\,m^{-1}\,K^{-1}$
Solid real density	2450	$kg\,m^{-3}$
Intrinsic permeability	$2\cdot10^{-20}$	m^2
Viscosity	$1\cdot10^{-3}$	Pa s
Time step size	10000	s
Young's modulus	5	GPa
Poisson's ratio	0.3	-
Biot coefficient	1	-
Fluid volumetric thermal expansion coefficient	$4\cdot10^{-4}$	K^{-1}
Solid linear thermal expansion coefficient	$4.5\cdot10^{-5}$	K^{-1}

Table 3. Parameters used in the numerical example

Parameter	Value	Unit
Initial temperature	293.15	K
Initial solid volume fraction	0.5	-
Water specific heat capacity	4179	$J\,kg^{-1}\,K^{-1}$
Water thermal conductivity	0.58	$W\,m^{-1}\,K^{-1}$
Water real density	1000	$kg\,m^{-3}$
Ice specific heat capacity	2052	$J\,kg^{-1}\,K^{-1}$
Ice thermal conductivity	2.2	$W\,m^{-1}\,K^{-1}$
Ice real density	920	$kg\,m^{-3}$
Solid specific heat capacity	900	$J\,kg^{-1}\,K^{-1}$
Solid thermal conductivity	1.1	$W\,m^{-1}\,K^{-1}$
Solid real density	2000	$kg\,m^{-3}$
Initial intrinsic permeability	10^{-12}	m^2
Viscosity	$1.278 \cdot 10^{-3}$	Pa s
Time step size	300	s
Lamé constant μ_I	4.17	GPa
Lamé constant λ_I	2.78	GPa
Lamé constant μ_S	12.5	GPa
Lamé constant λ_S	8.33	GPa

Accepted manuscript
doi: 10.1680/jenge.18.00092

Figure 1. Decomposition of the solid deformation gradient (reproduce from Graf (2008))

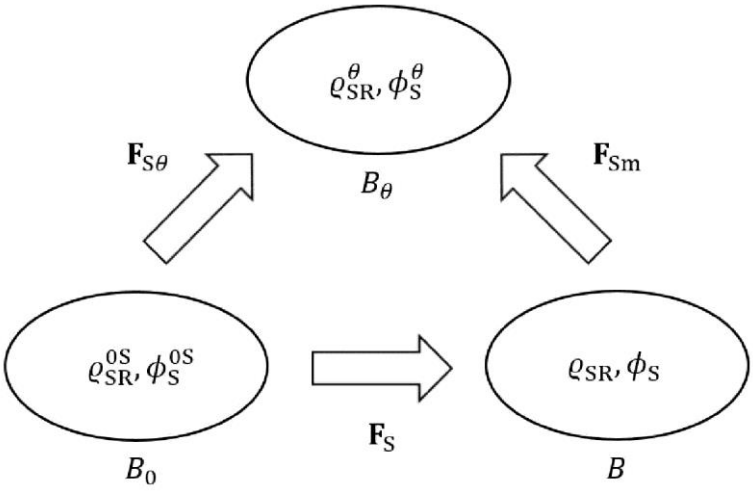

Accepted manuscript
doi: 10.1680/jenge.18.00092

Figure 2. Verification of the freezing wall benchmark

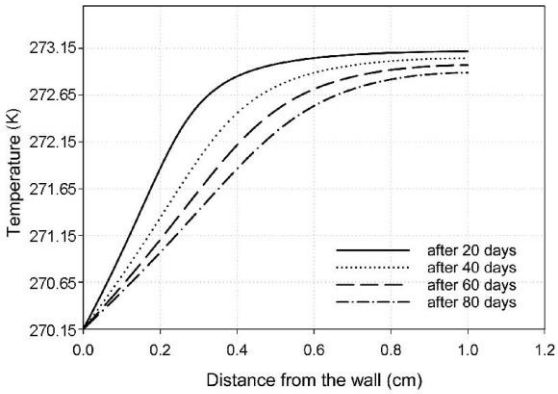

(a) The temperature profile during the freezing process

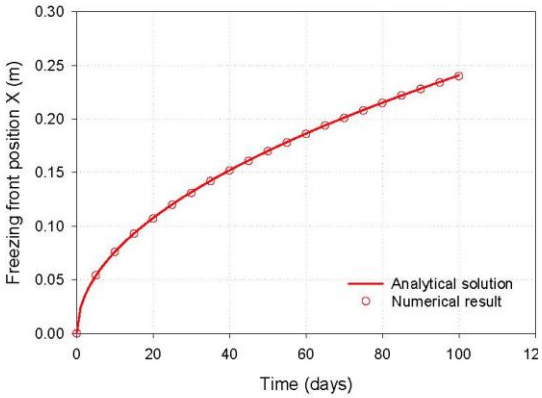

(b) The propagation of the freezing front over time.

Accepted manuscript
doi: 10.1680/jenge.18.00092

Figure 3. Model setup for the point heat source consolidation

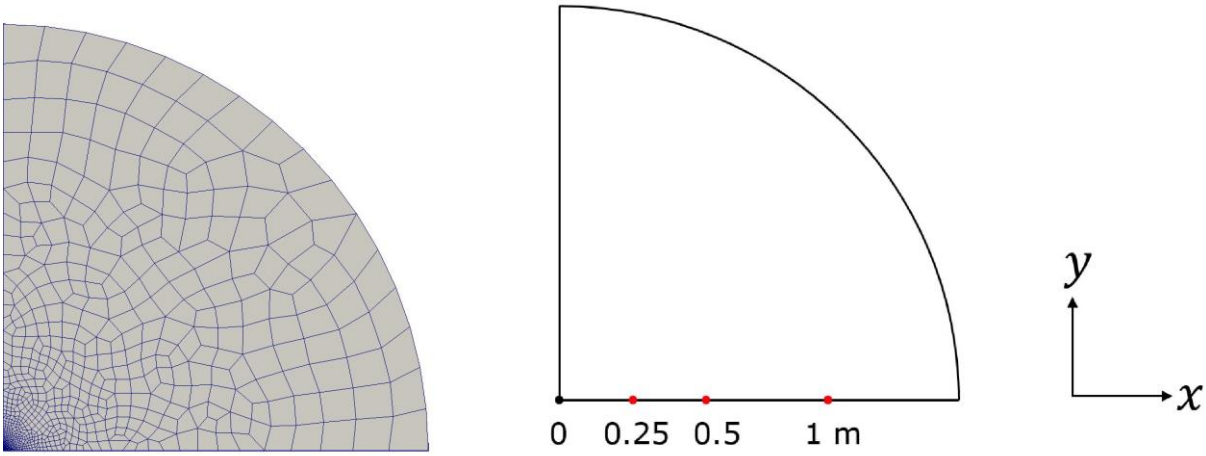

(a) Mesh distribution and domain

(b) Observation points in the domain

Accepted manuscript
doi: 10.1680/jenge.18.00092

Figure 4. The numerical solution compared with analytical solution for the point heat-source THM consolidation problem (temperature)

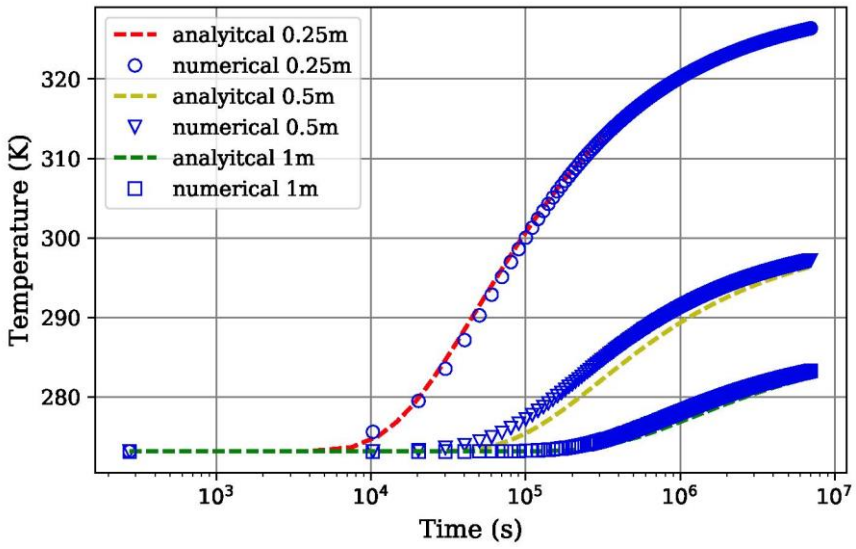

Accepted manuscript
doi: 10.1680/jenge.18.00092

Figure 5. The numerical solution compared with analytical solution for the point heat-source THM consolidation problem (pressure)

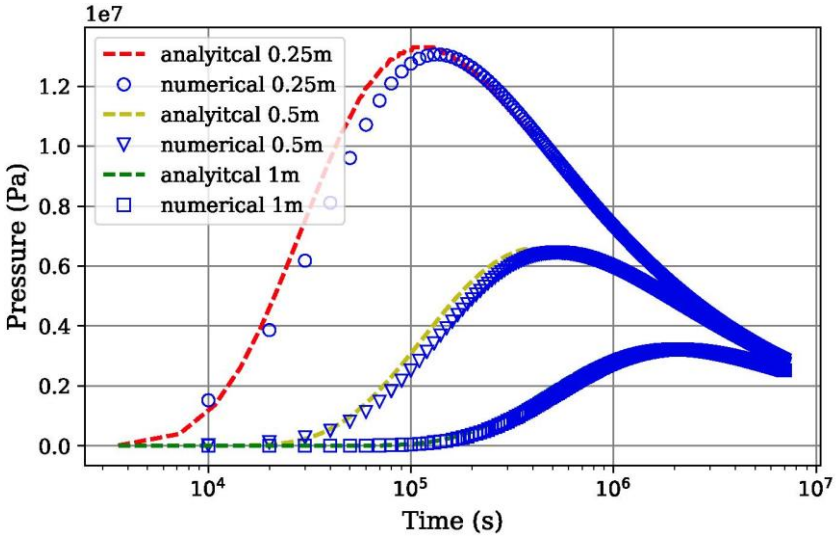

Accepted manuscript
doi: 10.1680/jenge.18.00092

Figure 6. The numerical solution compared with analytical solution (displacement)

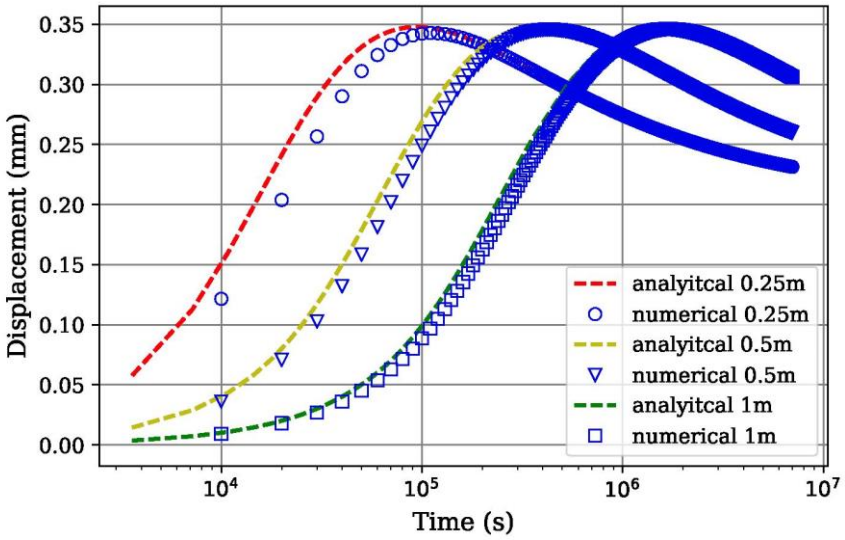

Accepted manuscript
doi: 10.1680/jenge.18.00092

Figure 7. Model setup for the CIF tests: (a) temperature profile; (b) boundary constraints

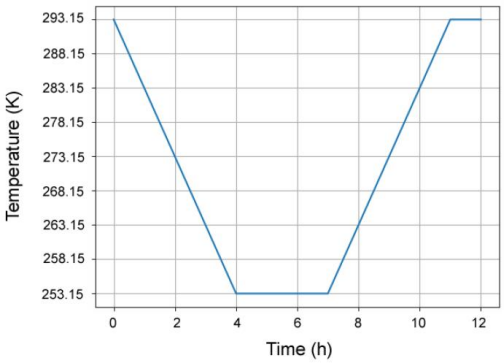

(a) Temperature load for the bottom boundary.

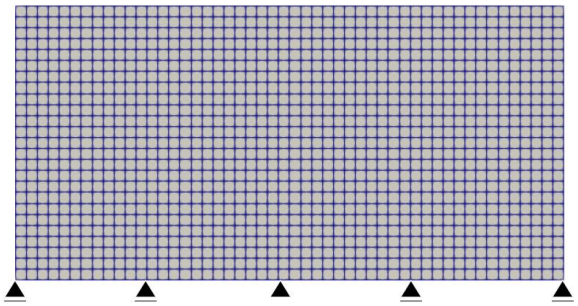

(b) Displacement boundary conditions and finite element mesh.

Accepted manuscript
doi: 10.1680/jenge.18.00092

Figure 8. Temperature, ice volume fraction and volume deformation after 5 and 11.8 hours. Displacements have been scaled by a factor of 10

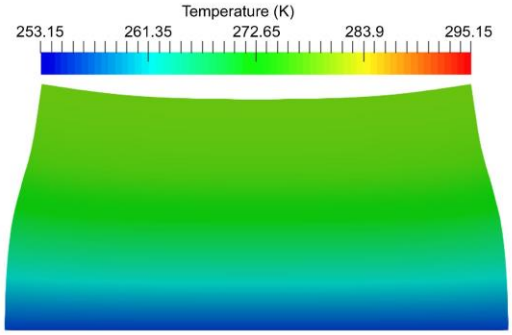

(a) Temperature at 5 hours

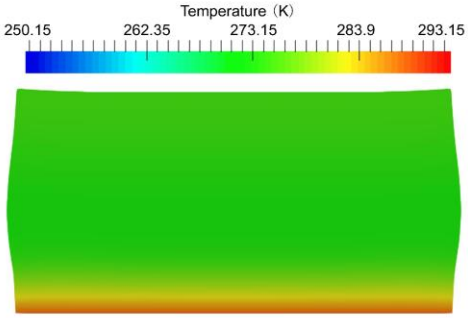

(b) Temperature at 11.8 hours

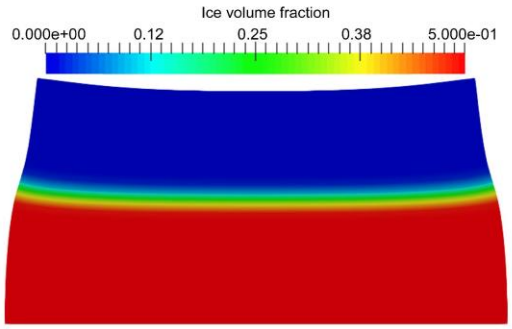

(c) Ice volume fraction at 5 hours

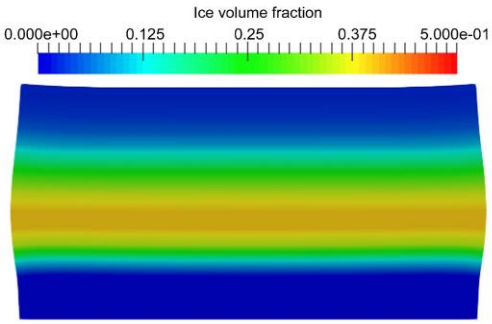

(d) Ice volume fraction at 11.8 hours

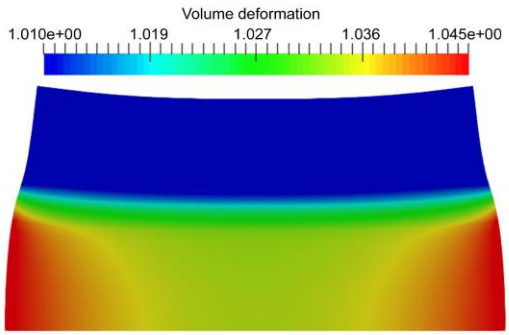

(e) Volume deformation at 5 hours

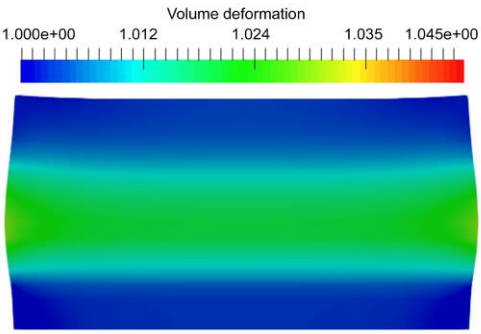

(f) Volume deformation at 11.8 hours

Accepted manuscript
doi: 10.1680/jenge.18.00092

Figure 9. Pressure distribution and velocity after 5 and 11.8 hours. Velocity vectors are scaled according to velocity magnitude

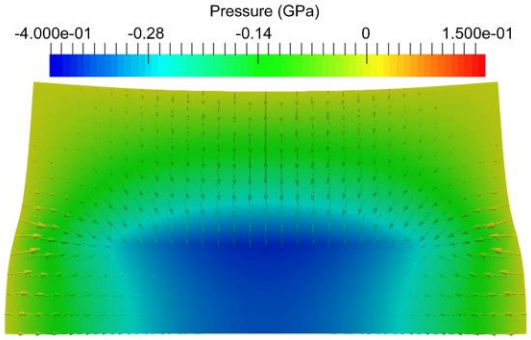

(a) Liquid pressure at 5 hours, constant permeability.

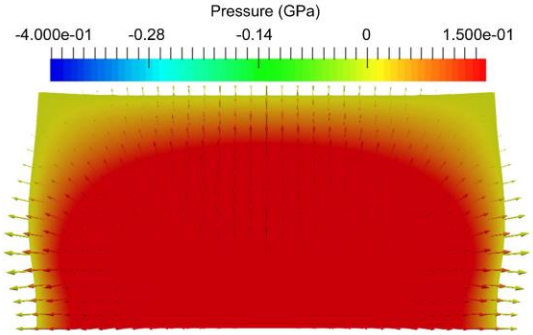

(b) Liquid pressure at 11.8 hours, constant permeability

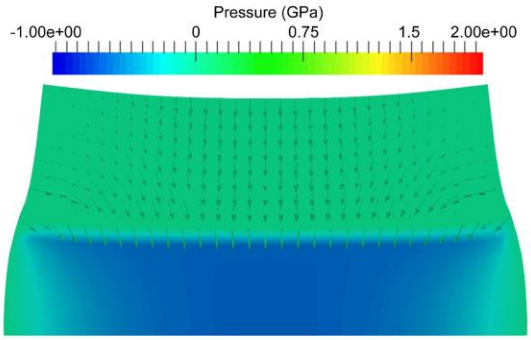

(c) Liquid pressure at 5 hours, variable permeability.

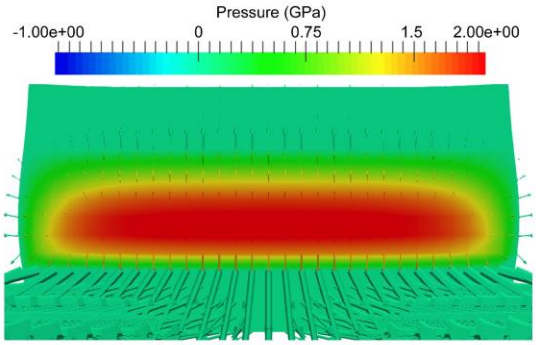

(d) Liquid pressure at 11.8 hours, variable permeability.